ARTICLE TYPE www. rsc.org/xxxxxx | XXXXXXXX

Cold heteromolecular dipolar collisions†

Brian C. Sawyer,*[a] Benjamin K. Stuhl,[a] Mark Yeo,[a] Timur V. Tscherbul,[b,c] Matthew T. Hummon,[a] Yong Xia,[a,d] Jacek Kłos,[e] David Patterson,[b] John M. Doyle,[b] and Jun Ye[a]

Received Xth XXXXXXXXXX 20XX, Accepted Xth XXXXXXXXX 20XX
First published on the web Xth XXXXXXXXXX 200X
DOI: 10.1039/b000000x

Cold molecules promise to reveal a rich set of novel collision dynamics in the low-energy regime. By combining for the first time the techniques of Stark deceleration, magnetic trapping, and cryogenic buffer gas cooling, we present the first experimental observation of cold collisions between two different species of state-selected neutral polar molecules. This has enabled an absolute measurement of the total trap loss cross sections between OH and ND_3 at a mean collision energy of 3.6 cm^{-1} (5 K). Due to the dipolar interaction, the total cross section increases upon application of an external polarizing electric field. Cross sections computed from *ab initio* potential energy surfaces are in good agreement with the measured value at zero external electric field. The theory presented here represents the first such analysis of collisions between a $^2\Pi$ radical and a closed-shell polyatomic molecule.

1 Introduction

For half a century, scattering of crossed atomic or molecular beams under single-collision conditions has remained the primary technique for investigation of inelastic and reactive dynamics at collision energies above ∼1 kcal/mol (∼500 K)[1]. Experiments using electric field-aligned neutral polar molecules can probe the steric asymmetry of atom-molecule[2–4] and bi-molecular[5,6] potential energy surfaces (PESs), but their large center-of-mass collision energies have precluded the observation of electric field modification of these potentials. However, in the cold collision regime where only tens of scattering partial waves contribute, one can move beyond molecular orientation and directly modify intermolecular dynamics via the long-range dipole interaction. The relatively low number densities (10^6-10^8 cm^{-3}) of cold molecule production techniques have thus far limited gas-phase collision experiments between state-selected distinct polar species to >300 K. We combine for the first time the methods of Stark deceleration, magnetic trapping, and buffer gas cooling to enhance molecular interaction time by $\sim 10^5$ and overcome this density limitation. Here we present the first observation of cold (5 K) heteromolecular dipolar collisions and describe the first theoretical study of scattering in the many partial-wave regime with chemically-relevant OH and ND_3 molecules.

The last decade has seen tremendous progress in the production of cold and ultracold polar molecules[7]. Application of these production techniques to the study of novel atom-molecule and molecule-molecule scattering has led gas-phase collision physics to new low temperature regimes. Specifically, crossed beam experiments using rare gas atoms and Stark decelerated OH ($^2\Pi$) molecules have allowed for the study of inelastic scattering at translational energies comparable to that of OH rotation (∼100 K)[8–10]. By measuring collisional loss of a magnetically trapped OH target with incident beams of He or D_2, we have determined total trap loss cross sections at similar energies[11,12]. Buffer gas cooling has been employed in the study of elastic and inelastic collisions of He-NH ($^3\Sigma$)[13,14] and He-TiO[15]. Cold reactive collisions have been observed using a velocity-filtered room-temperature beam of CH_3F colliding with trapped Ca^+ atomic ions[16]. In the ultracold regime[17], bimolecular chemical reactions between ground-state KRb molecules at temperatures of a few hundred nanoKelvin have been directly controlled via external electric fields[18,19], opening the door for experimental probes of quantum many-body effects in a dipolar molecular gas[20].

To observe dipolar collisions between state-selected OH and ND_3, we constructed a novel cold collision apparatus combining Stark decelerated and magnetically trapped OH with a continuous buffer gas cooled beam of ND_3, allowing in-

† Electronic Supplementary Information (ESI) available: Technical details concerning experimental calibration of absolute trap loss cross sections are provided. See DOI: 10.1039/b000000x/

[a] *JILA, National Institute of Standards and Technology and the University of Colorado, Department of Physics, University of Colorado, Boulder, Colorado 80309-0440, USA. Fax: 303-492-5235; Tel: 303-492-7789; E-mail: bsawyer@nist.gov*
[b] *Department of Physics, Harvard University, Harvard-MIT Center for Ultracold Atoms, Cambridge, Massachusetts 02138, USA*
[c] *ITAMP, Harvard-Smithsonian Center for Astrophysics, Cambridge, Massachusetts 02138, USA*
[d] *Department of Physics, East China Normal University, Shanghai 200062, China*
[e] *Department of Chemistry and Biochemistry, University of Maryland, College Park, MD 20742-2021, USA*

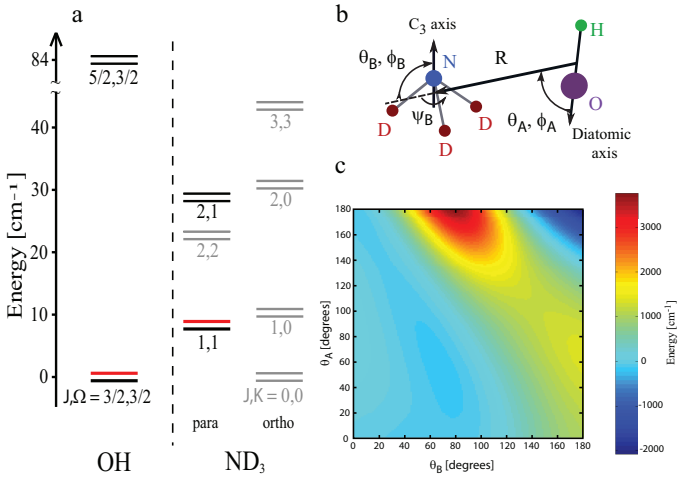

Fig. 1 (a) Rotational structure of OH and ND_3 molecules. The parity-doublet splitting of each rotational level has been expanded for clarity, while the black and red parity levels are the ones included in the OH-ND_3 scattering calculation. The parity states in red are those selected by the experimental apparatus for the cold collisions described herein. (b) Illustration of the Jacobi coordinates used for OH-ND_3 collision calculations. We define R as the distance between the molecular centers of mass while the Euler angles (θ_A, ϕ_A) and (θ_B, ϕ_B) give the orientation of the OH and ND_3 axes, respectively, in the body-fixed frame relative to R. The coordinate ψ_B specifies the orientation of the ND_3 monomer within the OH-ND_3 complex. The geometry $\phi_A = \phi_B = \theta_A = \theta_B = 0$ corresponds to the OH axis lying in the σ_v symmetry plane of ND_3 with the O atom facing the plane of D atoms. (c) Contour plot of the lowest adiabatic potential energy surface for the A'' state (in the C_s geometry) of the OH-ND_3 collision complex at $R = 3.1$ Å and $\phi_A = \phi_B = 0$ as a function of θ_A and θ_B. The color legend is scaled in units of cm^{-1}.

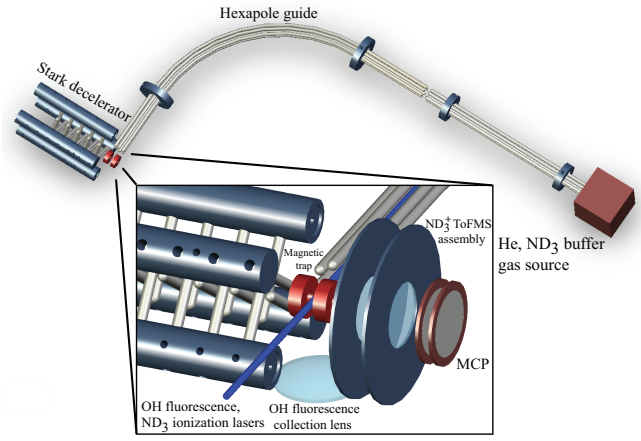

Fig. 2 Illustration of the combined Stark decelerator, magnetic trap, and buffer gas beam assembly. The curved hexapole filters cold ND_3 from the He buffer gas and guides the continuous beam to the OH magnetic trap. (Inset) Closeup of the trap assembly showing the dual-species detection components. We detect OH and ND_3 in the collision region using laser-induced fluorescence (LIF) and resonance-enhanced multiphoton ionization (REMPI), respectively. Hydroxyl fluorescence at 313 nm is collected using a lens mounted 2.5 cm below the magnetic trap center. Ionized ND_3^+ molecules are accelerated to a microchannel plate (MCP) detector by placing 950 V on the front magnet, 0 V on the back magnet, and -1100 V on the acceleration plates that make up a time-of-flight mass spectrometer.

teraction times of ∼1 s. In contrast to traditional scattering experiments, our measurement is sensitive to both inelastic and *elastic* collisions. Furthermore, fewer than 100 partial waves contribute to the 5 K collision — placing the OH-ND_3 interaction in an intermediate regime between gas-kinetic and quantum scattering. We report theoretical OH-ND_3 cross sections computed from *ab initio* potentials that are in good agreement with the measured zero-field trap loss cross section. Given the generality of buffer gas cooling and electro/magnetostatic velocity filtering, our apparatus allows for a large class of electric field dependent cold molecular collision studies.

Two readily coolable species, hydroxyl and ammonia, are ubiquitous in atmospheric and astrophysical spectroscopy. Large interstellar clouds of OH and NH_3 (some co-located) have been detected in both absorption and maser emission along microwave parity-doublets[21]. In the troposphere, hydroxyl-ammonia reactions are the dominant mechanism for removal of NH_3[22]. We choose to investigate electric field-dependent cold OH-ND_3 collisions due to the large static polarizability of both species and the near-degeneracy of the energy splittings of the OH Λ-doublet (0.056 cm^{-1}) and ND_3 inversion-doublet (0.053 cm^{-1}). The former allows for field orientation and precise control over the internal and external degrees of freedom of both molecules, while the latter has been shown to cause large enhancements in inelastic rates at room temperature[23]. Experimentally-relevant rotational and parity-doublet states of OH and ND_3 are illustrated in Fig. 1a.

2 Cold OH-ND_3 collision experiment

The experimental setup consists of two distinct cold molecule apparatus as shown in Fig. 2: a Stark decelerator/magnetic trap assembly[11,24] and a buffer-gas cooled continuous molecular beam source. A supersonic beam of OH molecules seeded in Kr is decelerated and trapped at a temperature of 70 mK and density of $\sim 10^6$ cm^{-3} as described in previous work[11]. Only those OH molecules residing in the $^2\Pi_{3/2}$ $|J, M_J, p\rangle = |\frac{3}{2}, +\frac{3}{2}, +\rangle$ ground state are phase-stably Stark decelerated and magnetically trapped. Here J, M_J, and p denote the total angular momentum, its projection on the external electric field axis, and the parity of the state in the absence of electric fields, respectively. To detect trapped OH, the molecules are excited at the 282 nm $A^2\Sigma^+(v=1) \leftarrow X^2\Pi_{3/2}(v=0)$ transition. Fluores-

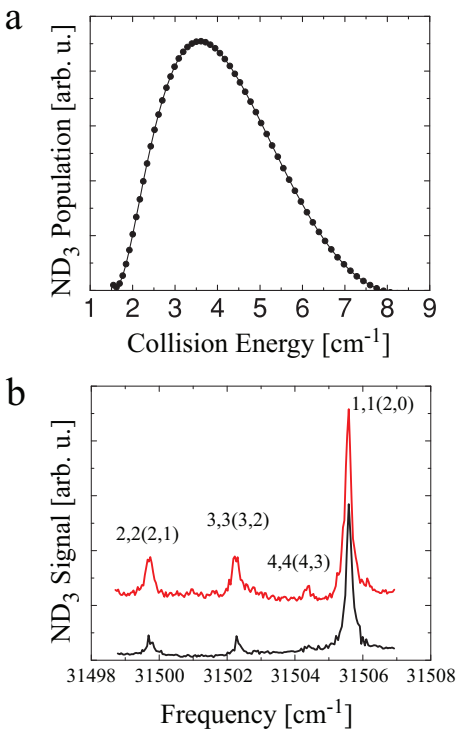

Fig. 3 (a) Translational energy spectrum of the guided continuous ND_3 beam as measured by 2+1 REMPI in the collision region. (b) Rotationally-resolved REMPI spectrum of guided ND_3 molecules showing different J,K states. The upper red curve (offset for clarity) was taken at buffer gas flows of 2.0 and 2.5 sccm of He and ND_3, respectively. The lower black curve displays the smaller rotational temperature observed at 3.5 and 1.0 sccm. Intermediate rotational levels in the excited $\tilde{B}(v_2 = 5)$ electronic state are labeled in parentheses for each transition.

cence from the 313 nm $A^2\Sigma^+(v=1) \rightarrow X^2\Pi_{3/2}(v=1)$ decay is collected by a lens mounted to the magnetic trap assembly.

We employ buffer gas cooling and Stark velocity filtering to generate a continuous beam of cold ND_3 molecules at a density of 10^8 cm^{-3} and mean velocity of 100 m/s. Our measured beam flux of 10^{11} s^{-1} is comparable to that of previous experiments[25,26]. Cold ND_3 is generated in a copper cell filled with He buffer gas at 4.5 K. A 6 mm-diameter aperture is cut into the front of the cell directly opposite the ND_3 inlet to allow the cold He/ND_3 mixture to escape. An electrostatic hexapole consisting of six 3 mm-diameter steel rods and possessing an inner diameter of 6 mm is mounted 2 mm from the cell aperture. This straight hexapole guide is 20 cm long and mounts to a 3 mm-thick gate valve that isolates the OH trap vacuum from the cryogenic vacuum. A curved hexapole is mounted just beyond the gate valve and follows a 90° bend at a radius of 13.5 cm. The hexapole guide terminates 1 cm from the permanent magnetic trap center. The curved hexapole filters cold ND_3 from the He buffer gas and sets an upper bound on the accepted forward velocity for weak-field seeking states (∼150 m/s at ±5 kV for $|J,K\rangle = |1,1\rangle$). The quantum numbers J and K denote the total molecular angular momentum and its projection on the ND_3 symmetry axis, respectively. Figure 3a displays the measured energy distribution of guided $|1,1\rangle$ ND_3 molecules in the OH-ND_3 center-of-mass frame. To quantify the continuous beam velocity, the hexapole is switched so that guided ND_3 flux can be measured over different guiding durations. After including the guide path length, we differentiate a fit of the resulting curve to obtain the ND_3 velocity distribution of Fig. 3a. Guided ND_3 is detected in the collision region using 2+1 resonance-enhanced multiphoton ionization (REMPI)[27] and subsequent ion detection. To accomplish this, ND_3 in the $|1,1\rangle$ state is resonantly ionized between the trap magnets using a focused 317.4 nm, 10 ns laser pulse. To accelerate ions to a microchannel plate (MCP) detector (see Fig. 2), the trap magnets are charged to a potential difference of 950 V. After extraction from the trap, ions enter a 2 cm long field-free region and are subsequently detected by the MCP.

Our dual-detection scheme permits characterization of the state purity of both OH and ND_3. Due to the state selectivity of Stark deceleration and magnetic trapping, perfect OH rotational, Λ-doublet, and hyperfine state purity is achieved. Vibrationally excited ($v=1$) OH are phase stably decelerated with $v=0$ molecules, but <5% of OH are initially produced in the $v=1$ state[28]. We also characterize the ND_3 rotational distribution within the collision region. The rotational structure of ND_3 is shown in Fig. 1a while Fig. 3b displays the measured rotational spectra of guided ND_3 molecules for two different buffer gas flows: 2.0 sccm He and 2.5 sccm ND_3 (upper curve) and 3.5 sccm He and 1.0 sccm ND_3 (lower curve). A standard cubic centimeter per minute (sccm) is equivalent to 4.4×10^{17} s^{-1}. As the ratio of He to ND_3 flow is increased, the two-state ($|1,1\rangle, |2,2\rangle$) rotational temperature drops from 6.3 K to 5.4 K. With the larger He:ND_3 flow ratio, the relative guided populations of anti-symmetric (weak-field seeking) $|1,1\rangle$, $|2,2\rangle$, $|3,3\rangle$, and $|4,4\rangle$ states are 87%, 9%, 4%, and <1%, respectively. This ground state fraction is similar to that measured by depletion spectroscopy of a buffer gas cooled H_2CO beam[25]. States with $K=0$ do not exhibit a first-order Stark shift and are not guided. Also, at this flow and guide voltage (±5 kV), no population is observed in those states where $J \neq K$. Our choice of 3.5/1.0 sccm for the collision experiment is a compromise between maximizing $|1,1\rangle$ flux while minimizing rotational temperature.

To quantify total trap loss cross sections between OH and ND_3, it is necessary to measure both collision-induced OH trap loss and absolute colliding ND_3 density. Loss of trapped OH is measured as shown in Fig. 4a over a period of 160 ms. First, the background-gas limited trap decay rate (γ_{off}) is mea-

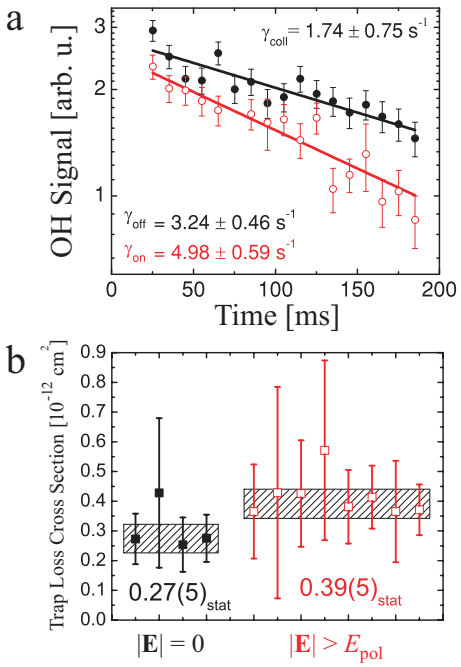

Fig. 4 (a) Semi-logarithmic plot of OH trap decay rates with (○) and without (●) the colliding ND_3 beam. The decay rate due solely to cold OH-ND_3 collisions is $\gamma_{coll} = \gamma_{on} - \gamma_{off}$. (b) Plot of all experimental runs measuring total cross sections with (□) and without (■) a polarizing electric field. Average cross sections are determined from the weighted mean of all points and errors for the given E-field condition. The cross-hatched regions represent one statistical standard error. Individual error bars for each experimental run are obtained by propagating the standard deviation from exponential fits of γ_{on} and γ_{off} to γ_{coll}.

sured with the ND_3 flow off. This decay rate is determined by a single-exponential fit to the data. The value of γ_{off} is set by the presence of residual Kr in the trap chamber and is typically 2-3 s^{-1} at a pulsed-valve repetition rate of 5 Hz. The cold ND_3 beam is then turned on and the loss rate due to background gas plus cold ND_3 (γ_{on}) is measured. The collision-induced loss rate (γ_{coll}) is the difference of the two rates. This differential measurement makes γ_{coll} insensitive to day-to-day variations in background pressure, and yields a single-measurement fractional error of ∼30-40% in the available runtime of 1 hr‡. To investigate the effect of an external electric field on the cross section, we apply two distinct electric field configurations to the colliding molecules. We define the polarizing electric field for a given molecule as $E_{pol} = \Delta/2\mu$ where μ is the molecular permanent dipole moment and Δ is the parity-doublet splitting (E_{pol}=1.7 kV/cm for OH and 2.0 kV/cm for ND_3). For both field distributions, $E > 2$ kV/cm throughout the collision region, polarizing both colliding species. One E-field distribution is produced by charging the trap magnets themselves and lowers the OH radial trap depth by ∼20% due to the relative orientations of E- and B-fields within the collision region. The alternate field distribution is created by charging a stainless steel cup placed between the rear trap magnet and time-of-flight mass spectrometer. The resulting distinct distribution between the grounded magnets increases the radial trap depth by ∼40%. Polarization of OH and ND_3 under both field configurations is experimentally verified in the collision region through spectroscopic measurement of the population of cold ND_3 molecules in the strong-field seeking (unguided) $|1,1\rangle$ state. This population is measured as a direct result of inversion-state mixing under the polarizing electric fields and is not detected in the absence of either electric field configuration. We observe no difference in collisional loss between these two configurations, and thus the changes in trap loss arise directly from the enhanced dipolar interactions between OH-ND_3 under the applied E-field.

To determine the value of the loss cross section, σ_{exp}^{loss}, we use REMPI to calibrate the absolute density of the continuous ND_3 beam within the collision region for each measurement of γ_{coll}. Conversion of MCP output current to absolute molecule density is notoriously difficult due to unknown ionization volume/efficiency and uncertain MCP gain. To sidestep these issues, a leak valve and calibrated quadrupole mass spectrometer are used to admit a known pressure of 295 K ND_3 gas into the trap chamber. The measured ND_3 pressure is then scaled down by the Boltzmann fraction of molecules in the $|1,1\rangle$ antisymmetric state at thermal equilibrium ($4.45\text{x}10^{-3}$), and an absolute ND_3 density is assigned to the observed MCP output current. Provided the cold beam is much larger than the ionization volume (true in our system), this calibration procedure is insensitive to the above problems. We also correct for overlap of REMPI transitions in the 295 K ND_3 spectrum†. The relatively small rotational energy splittings of ND_3 displayed in Fig. 1a lead to a congested spectrum at room temperature. Failure to account for overlap of transitions through the intermediate $\tilde{B}(v_2 = 5)$ state would lead to an underestimate of the cold beam density and concomitant overestimate of cross sections. Finally, a total trap loss cross section is determined for each experimental run as $\sigma_{exp}^{loss} = \gamma_{coll}(n_0 v_{rel})^{-1}$, where n_0 is the measured density of ND_3 and v_{rel} is the mean relative molecule velocity.

‡ Given that ammonia freezes below 195 K, ice formation within the buffer gas cell is unavoidable. However, we achieve stable beam operation over >1 hour by maximizing the distance (>1 cm) between the warm ND_3 inlet and cold cell walls. When ND_3 ice finally bridges the gap between the cell wall and warm inlet, sudden vaporization of the ice causes a large pressure rise in the cell and surrounding chamber which leads to significant cell heating and loss of cold beam flux. Charcoal sorb (∼2000 cm^2) at 4.5 K is used to pump He gas within the dewar vacuum.

3 Quantum theory of OH-ND_3 collisions

3.1 *Ab initio* calculations

A complete theoretical description of the OH-ND_3 collision at 5 K is complicated by the $^2\Pi$ symmetry of ground-state hydroxyl. Interactions including Π molecules are characterized by multiple electronic potentials, avoided crossings, and conical intersections. As such, scattering calculations based on *ab initio* potential energy surfaces have thus far been limited to Σ molecules[29,30] or collisions between Π molecules and rare gas atoms or closed-shell diatomics with simple rotational structure[31,32]. A full description of the theory results summarized here will be published elsewhere[33].

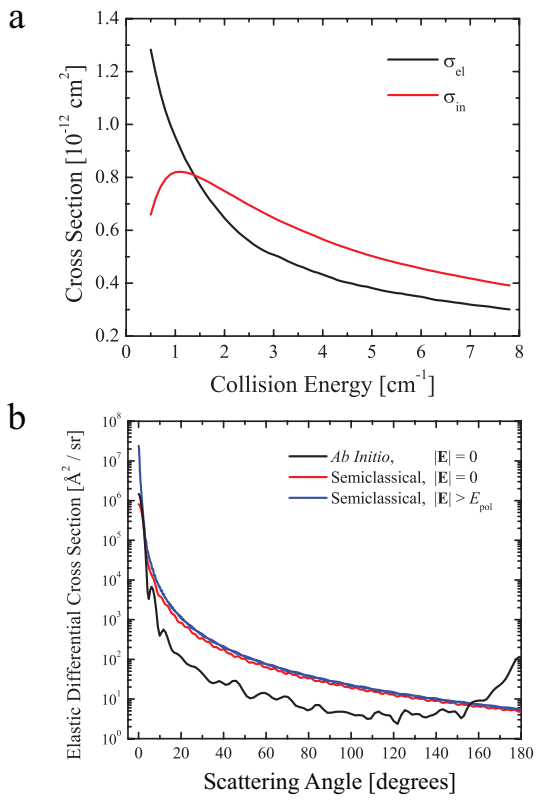

Fig. 5 Theoretical OH-ND_3 integral and differential cross sections. (a) Plot of theoretical OH-ND_3 elastic (σ_{el}) and inelastic (σ_{in}) cross sections as obtained from the *ab initio* PESs. (b) Semi-logarithmic plot of the theoretical differential cross sections for 5 K elastic OH-ND_3 collisions in units of $Å^2/sr$. Results from both *ab initio* and semiclassical analysis are given. These curves are used to calculate the σ^{loss}_{theory} and σ^{loss}_{sc} values of Table 1 from free-space elastic and inelastic cross sections by integrating from $\theta_{min} = 13°$. In the presence of an external E-field, the DCS becomes more strongly forward-peaked reflecting collisions at larger impact parameter.

To describe the OH-ND_3 collision complex, we calculate the two lowest adiabatic PESs (corresponding to the A' and A'' symmetries in the C_s geometry of the complex) using a spin-Restricted Coupled Cluster method with Single, Double, and non-iterative Triple excitations (RCCSD(T)) as implemented in MOLPRO[34]. For non-planar geometries of the complex ($\phi \neq 0$), we calculate the adiabatic PESs and the adiabatic-to-diabatic transformation angle using a multireference self-consistent field approach[35]. The lowest adiabatic PES (V_1) is calculated using the RCCSD(T) method and the excited PES (V_2) is calculated by adding the energy difference $\Delta V = V_2 - V_1$ evaluated at the MRCISD+Q level (multireference configuration interaction with single, double and Davidson correction for higher excitations)[35].

An augmented correlation-consistent triple zeta basis (aug-cc-pVTZ) is used for both N and O atoms[36]. As illustrated in Fig. 1b, we define R as the distance between the molecular centers of mass while the Euler angles (θ_A, ϕ_A) and (θ_B, ϕ_B) give the orientation of the OH and ND_3 axes, respectively, in the body-fixed frame relative to R. A third angle, ψ_B, gives the orientation of the ND_3 monomer about its C_3 symmetry axis. Figure 1c shows the lowest adiabatic PES of A'' symmetry as a function of the orientation angles θ_A and θ_B for $R = 3.1$ Å and $\phi = 0$. Following the diagonal line defined by $\theta_A = \theta_B$, a barrier of $\sim$1000 cm^{-1} is observed between head-to-tail $ND_3\cdots OH$ and $D_3N\cdots HO$ configurations, demonstrating the large anisotropy of the OH-ND_3 interaction.

To elucidate the dynamics of cold OH-ND_3 collisions, we develop and implement a rigorous quantum scattering approach based on the close-coupling (CC) expansion of the wave function of the collision complex using the total angular momentum representation in the body-fixed coordinate frame. The Hamiltonian of the OH + ND_3 collision complex may be written (in atomic units)

$$\hat{H} = -\frac{1}{2\mu R}\frac{\partial^2}{\partial R^2}R + \frac{(\hat{J}_{tot} - \hat{J}_A - \hat{J}_B)^2}{2\mu R^2} + \sum_{\Lambda,\Lambda'} V_{\Lambda\Lambda'}(R, \mathbf{\Omega}_A, \mathbf{\Omega}_B)|\Lambda\rangle\langle\Lambda'| + \hat{H}_{as}, \quad (1)$$

where μ and J_{tot} are the reduced mass and the total angular momentum of the collision complex, $\hat{J}_A$ and $\hat{J}_B$ are the total angular momenta of OH and ND_3, $\boldsymbol{R}$ is the vector pointing from the center of mass of OH to that of ND_3 (see Fig. 1b), and $|\Lambda\rangle$ are the diabatic electronic basis functions[35]. The Euler angles $\mathbf{\Omega}_A$ and $\mathbf{\Omega}_B$ specify the orientation of molecule-fixed (MF) axes attached to OH and ND_3 relative to the body-fixed (BF) frame with the z-axis along $\boldsymbol{R}$. The asymptotic Hamiltonian $\hat{H}_{as} = \hat{H}_A + \hat{H}_B$ describes non-interacting collision partners and includes the intramolecular spin-orbit and Λ-doubling terms for OH[37] and the inversion term for ND_3[38]. The matrix elements of the asymptotic Hamiltonian $\hat{H}_{as}$ are

parameterized by the accurate spectroscopic constants of OH and ND_3 [37,38].

To solve the scattering problem, we expand the wave function of the collision complex in a complete orthonormal basis of angular functions, which includes the Wigner D-functions describing the overall rotation of the collision complex, Hund's case (a) basis functions $|J_A M_A \Omega_A\rangle|\Lambda\Sigma\rangle$ for $OH(^2\Pi)$, and symmetric-top basis functions of definite parity $|J_B M_B K_B \varepsilon_B\rangle$ for ND_3 [33]. Here, M_A (Ω_A) are the BF (MF) projections of J_A and M_B (K_B) are the BF (MF) projections of J_B. The radial expansion coefficients and S-matrix elements are obtained by numerical integration of the CC equations using the modified log-derivative algorithm [39] from $R = 4\,a_0$ to $R = 200\,a_0$ with a grid step of 0.1 a_0. The scattering basis set includes all rotational, Λ-doublet, and inversion states of OH and ND_3 with $J_A \leq 3/2$, $|\Omega_A| = 1/2, 3/2$ and $J_B \leq 2$, $K_B = 1$, resulting in 320 CC equations for $J_{\rm tot} > 4$. We note that the anisotropy of the OH-ND_3 interaction potential with respect to the rotation of ND_3 about its symmetry axis couples basis functions with different K_B. This anisotropy was neglected in our *ab initio* calculations, so only $K_B = 1$ functions were included in the basis set expansion. Scattering calculations were carried out for 135 values of $J_{\rm tot}$ between $1/2$ and $270/2$. Test calculations with larger rotational basis sets and $J_{\rm tot} > 270/2$ indicate that the cross sections are converged to within 5% in the range of collision energies $0.5 - 8$ cm^{-1}.

The diabatic PESs $V_{\Lambda\Lambda'}(R, \mathbf{\Omega}_A, \mathbf{\Omega}_B)$ in Eq. 1 are evaluated from the two lowest adiabatic PESs and the adiabatic-to-diabatic transformation angle as described in Ref. 35. In these calculations, the OH and ND_3 interatomic distances are fixed at their corresponding equilibrium geometries: $r_{\rm OH} = 1.833\,a_0$ [37] and $r_{\rm ND3} = 1.915\,a_0$, respectively, and the DND angle is set to 112.249°. The geometry of the ND_3 monomer is optimized at the CCSD(T)/aug-cc-pVQZ level of theory. The diabatic PESs are expanded in angular basis functions $A^{\Lambda\Lambda'}_{\lambda_A\lambda_B\lambda\mu_B}(\mathbf{\Omega}_A, \mathbf{\Omega}_B)$ as [35]

$$V_{\Lambda\Lambda'}(R, \mathbf{\Omega}_A, \mathbf{\Omega}_B) = \sum_{\lambda_A,\lambda_B,\lambda} \sum_{\mu_B} V^{\Lambda\Lambda'}_{\lambda_A\lambda_B\lambda\mu_B}(R) A^{\Lambda\Lambda'}_{\lambda_A\lambda_B\lambda\mu_B}(\mathbf{\Omega}_A, \mathbf{\Omega}_B). \quad (2)$$

A model four-term parametrization of the OH-ND_3 PESs is constructed by restricting the expansion of Eq. 2 to the first few terms with $\Lambda = \Lambda'$ and $\lambda_A, \lambda_B = 0$ and 1 [40]. Setting $\psi_B = 0$ in Eq. 2 and using explicit expressions for the angular basis functions $A^{\Lambda\Lambda'}_{\lambda_A\lambda_B\lambda\mu_B}(\mathbf{\Omega}_A, \mathbf{\Omega}_B)$ [35], we obtain the radial expansion coefficients $V_{000}(R)$, $V_{112}(R)$, $V_{011}(R)$, and $V_{101}(R)$ from the lowest PES of A' symmetry evaluated in four reference geometries specified by $\theta_A = 0, \pi$, $\theta_B = 0, \pi$, and $\phi = 0$ [40]. In the limit $R \to \infty$, the coefficient $V_{112}(R) \propto R^{-3}$ incorporates the long-range dipolar interaction between OH and ND_3. All other coefficients go to zero as R^{-n} with $n > 3$, so our model PES correctly reproduces both the short-range isotropic and long-range anisotropic behavior of the OH-ND_3 interaction [35]. Test calculations show that omission of the short-range anisotropic terms $V_{011}(R)$ and $V_{101}(R)$ from scattering calculations does not modify the calculated cross sections by more than 15%.

The cross sections for OH trap loss are evaluated by summing and averaging the scattering amplitude over the internal states of ND_3, which are not monitored in the experiment

$$\sigma^{\rm loss}_{\gamma_A m_A \to \gamma'_A m'_A} = 2\pi \sum_{m_A} \sum_{\gamma'_B, m'_B} \int_{\theta_{\rm min}}^{\pi} d\theta \sin\theta \, \sigma_{\gamma_A m_A \gamma_B m_B \to \gamma'_A m'_A \gamma'_B m'_B}(\theta) \quad (3)$$

where γ_A and γ_B refer collectively to the rotational, Λ-doublet, and inversion states of OH and ND_3, m_A and m_B are the projections of J_A and J_B on the beam axis, and $\sigma_{\gamma_A m_A \gamma_B m_B \to \gamma'_A m'_A \gamma'_B m'_B}(\theta)$ is the state-to-state DCS as a function of the center-of-mass scattering angle θ. From Eq. 3, we obtain the total elastic and inelastic cross sections for trap loss as $\sigma^{\rm loss}_{\rm el} = \sigma^{\rm loss}_{\gamma_A \frac{3}{2} \to \gamma_A \frac{3}{2}}$ and $\sigma^{\rm loss}_{\rm inel} = \sum_{\gamma'_A \neq \gamma_A, m'_A \neq \frac{3}{2}} \sigma^{\rm loss}_{\gamma_A \frac{3}{2} \to \gamma'_A m'_A}$ for OH molecules initially in the Zeeman state $\gamma_A = |J_A = 3/2, m_A = 3/2, f\rangle$.

The cutoff angle $\theta_{\rm min}$ in Eq. 3 is given by [12]

$$\cos\theta_{\rm min} = \frac{1}{r_{\gamma_A\gamma'_A}} \left[1 - \frac{1}{2E_C} \left(\frac{M}{M_B} (U_{\gamma'_A m'_A} - E_{\gamma_A m_A}) - \Delta\varepsilon_{\gamma_A\gamma'_A} \right) \right], \quad (4)$$

where $M = M_A + M_B$ is the total mass, $r_{\gamma_A\gamma'_A} = (1 + \Delta\varepsilon_{\gamma_A\gamma'_A}/E_C)^{1/2}$, $\Delta\varepsilon_{\gamma_A\gamma'_A}$ is the energy gap between the initial and final Zeeman states ($\Delta\varepsilon_{\gamma_A\gamma'_A} > 0$ for the relaxation collisions considered in this work), $E_{\gamma_A m_A}$ is the average kinetic energy of trapped OH molecules, E_C is the collision energy, and $U_{\gamma'_A m'_A}$ is the trap depth. Equation 4 establishes that $\theta_{\rm min}$ increases with trap depth. Typical values of $\theta_{\rm min}$ range from zero (for inelastic collisions changing the sign of m_A) [12] to $\theta_{\rm min} = 13°$ (for elastic collisions) at $E_C = 5$ K and $E_{\gamma_A m_A} = 70$ mK. The calculated DCSs are strongly peaked in the forward direction ($\theta = 0$), so the elastic cross sections for trap loss in OH-ND_3 collisions are extremely sensitive to $\theta_{\rm min}$: we find that varying the trap depth from zero to 240 mK causes $\sigma^{\rm loss}_{\rm el}$ to decrease by a factor of $\sim$25. The elastic DCS is shown in Fig. 5b.

The CC equations are solved numerically to produce converged S-matrix elements and scattering cross sections for collision energies between 0.5 and 8 cm^{-1}, which are convoluted with the beam distribution function shown in Fig. 3a to enable direct comparison with experimental data. The cross sections for trap loss are evaluated by integrating the differential cross section (DCS) over a restricted angular range $[\theta_{\rm min}, \pi]$. The cutoff angle $\theta_{\rm min}$ serves to subtract contributions from forward-scattered elastic collision products that do not have enough kinetic energy to leave the trap [11,12,41].

3.2 Semiclassical Estimates

In the absence of rigorous field-dependent *ab initio* PESs for the OH-ND_3 complex, we provide semiclassical estimates of the OH trap loss cross sections at 5 K. We make use of the Eikonal approximation and Langevin capture model to compute elastic and inelastic OH-ND_3 cross sections, respectively. Within the Eikonal approximation, one assumes that scattering particles maintain a straight-line path throughout the collision process. This approximation is valid when the collision energy is larger than the scattering potential[42]. The Langevin capture model for inelastic collisions assumes that only those collision impact parameters within the centrifugal barrier lead to inelastic loss[43]. In the absence of an external electric field, we assume an isotropic and attractive van der Waals potential of the form

$$V(r) = -\frac{C_6}{r^6} \tag{5}$$

where r is the intermolecular distance and $C_6 = 21,380$ a.u. is computed from the dynamic polarizabilities of OH (α_{OH}) and ND_3 (α_{ND3}) according to[44]

$$C_6 = \frac{3}{\pi}\int_0^\infty \alpha_{\mathrm{OH}}(i\omega)\alpha_{\mathrm{ND3}}(i\omega)d\omega. \tag{6}$$

For collisions in the presence of the E-field, we add to the van der Waals potential an isotropic dipole interaction to obtain

$$V(r) = -\frac{C_6}{r^6} - \frac{C_3}{r^3} \tag{7}$$

where $C_3 = \langle\mu_{OH}\rangle\langle\mu_{ND3}\rangle$ consists of the expectation values of the OH and ND_3 permanent electric dipoles, respectively.

The elastic DCS for each intermolecular potential is computed as

$$\frac{d\sigma}{d\Omega} = |f(\theta)|^2 \tag{8}$$

where the energy-dependent scattering amplitude $f(\theta)$ is calculated numerically from[42]

$$f(\theta) = -ik\int_0^\infty bJ_0(kb\theta)[e^{2i\Delta(b)} - 1]db, \tag{9}$$

$$\Delta(b) \equiv -\frac{\mu}{2k}\int_{-\infty}^{+\infty} V(\sqrt{b^2+z^2})dz. \tag{10}$$

Here k is the center-of-mass collision wave vector, b is the impact parameter, μ is the reduced mass, and J_0 is the zeroth-order Bessel function of the first kind. Averaging over the measured collision energies of Fig. 3a, we then integrate the elastic DCSs of Fig. 5b over the restricted angular range $[\theta_{\mathrm{min}}, \pi]$ to include the effect of trap confinement as described in Section 3.1. Since inelastic collisions leave OH molecules untrapped and necessarily lead to loss, only energy-averaged integral inelastic cross sections are computed as in Ref. 43.

4 Results and Discussion

The measured total trap loss cross sections are displayed in Fig. 4b. Each point represents a distinct cross section measurement and the average results for zero and non-zero electric field are determined as the weighted mean of each data set. The cross-hatched areas illustrate one statistical standard error centered at the weighted mean of each set. In addition to the statistical error, we estimate that the ND_3 leak pressure calibration, 295 K REMPI line-overlap correction, and our use of $v_{\mathrm{rel}} = 100$ m/s in obtaining $\sigma_{\mathrm{exp}}^{\mathrm{loss}}$ add a common 19% systematic uncertainty to both absolute measurements. We attribute the largest contribution to systematic error to the line-overlap correction factor[†]. These experimental average values and errors for trap loss cross sections are given in the second column of Table 1. We observe enhancement of $\sigma_{\mathrm{exp}}^{\mathrm{loss}}$ by a factor of 1.4(3) when both molecules are polarized by an external E-field. This signals an increase of the total cross section ($\bar{\sigma}_{\mathrm{el}} + \bar{\sigma}_{\mathrm{in}}$) since experimentally we observe no dependence of loss on trap depth.

Figure 5a shows the calculated cross sections for elastic scattering and inelastic relaxation in OH-ND_3 collisions as functions of collision energy. These curves are computed from the zero-field *ab initio* PESs. The cross sections are extremely large, exceeding typical gas-kinetic values by orders of magnitude. This dramatic enhancement is a direct manifestation of the dipolar interaction, which induces direct couplings between the opposite parity levels. Because of the long-range couplings, both elastic and inelastic cross sections are dominated by collisions occurring at large impact parameters. A partial-wave analysis of the cross sections at 5 K reveals contributions from as many as 90 partial waves, and the dependences $\sigma_{\mathrm{el}}(J_{\mathrm{tot}})$ and $\sigma_{\mathrm{in}}(J_{\mathrm{tot}})$ peak at $J_{\mathrm{tot}} = 30.5$ and $J_{\mathrm{tot}} = 50.5$, respectively, where J_{tot} is the total angular momentum of the collision complex.

A more detailed theoretical analysis in the absence of external fields shows that the inelastic cross section associated with both OH and ND_3 changing their parity-doublet state is more than 6 times that for only one partner changing state. This propensity rule follows from the symmetry properties of the matrix elements of the dipolar interaction in the scattering basis. Table 1 compares the measured and theoretical trap loss cross sections. The $\sigma_{\mathrm{theory}}^{\mathrm{loss}}$ number is calculated using the OH-ND_3 elastic differential cross section (DCS) of Fig. 5b and includes the recently-elucidated effect of trap confinement on measured collisional loss at low momentum transfer[11,12,41]. Since glancing elastic collisions can leave scattered OH trapped, the measured $\sigma_{\mathrm{exp}}^{\mathrm{loss}}$ must be compared with $\sigma_{\mathrm{theory}}^{\mathrm{loss}} = \bar{\sigma}'_{\mathrm{el}} + \bar{\sigma}_{\mathrm{in}}$, where $\bar{\sigma}_{\mathrm{in}}$ is the velocity-averaged inelastic cross section and $\bar{\sigma}'_{\mathrm{el}}$ is the velocity-averaged elastic loss cross section that includes the trap loss suppression effect ($\bar{\sigma}'_{\mathrm{el}}/\bar{\sigma}_{\mathrm{el}} = 0.04$). The forward-peaked structure of the OH-

Table 1 Theoretical and experimental trap loss cross sections in units of 10^{-12} cm^2 (numbers in parentheses represent combined statistical and systematic errors). The $\sigma^{\rm loss}_{\rm theory}$ and $\sigma^{\rm loss}_{\rm sc}$ values include the effect of reduced elastic loss from glancing collisions due to trap confinement. The quantity $\bar{\sigma}_{\rm el}$ ($\bar{\sigma}_{\rm in}$) is the theoretical elastic (inelastic) cross section in the absence of trapping potentials and averaged over the experimental collision energy distribution of Fig. 3a.

	Experiment	Semiclassical	*Ab Initio*		
$\lvert\mathbf{E}\rvert$	$\sigma^{\rm loss}_{\rm exp}$	$\sigma^{\rm loss}_{\rm sc}$	$\sigma^{\rm loss}_{\rm theory}$	$\bar{\sigma}_{\rm el}$	$\bar{\sigma}_{\rm in}$
0	0.27(8)	0.28	0.59	0.44	0.57
$> E_{\rm pol}$	0.39(9)	0.32	-	-	-

ND_3 DCS is responsible for this large reduction in elastic loss.

From the semiclassical analysis of Section 3.2, we obtain zero-field elastic and inelastic cross sections of $\bar{\sigma}^{C6}_{\rm Eik} = 0.55 \times 10^{-12}$ cm^2 and $\bar{\sigma}^{C6}_{\rm L} = 0.18 \times 10^{-12}$ cm^2, respectively. Using the dipole potential of Eq. 7, we obtain $\bar{\sigma}^{\rm C6,C3}_{\rm Eik} = 1.5 \times 10^{-12}$ cm^2 and $\bar{\sigma}^{C6,C3}_{\rm L} = 0.19 \times 10^{-12}$ cm^2. From the elastic differential cross sections obtained within the Eikonal approximation, we also compute the elastic loss coefficients ($\bar{\sigma}'_{\rm el}/\bar{\sigma}_{\rm el}$) of 0.19 for the pure van der Waals potential and 0.09 for the combined potential of Eq. 7 (both at $\theta_{\rm min} = 13^\circ$). We therefore predict a factor of $\sim$1.14 enhancement in the measured total loss cross section when both species are polarized — in agreement with the measured value of 1.4(3). Furthermore, as shown in Table 1, the absolute values of these estimated trap loss cross sections are in excellent agreement with the the measured values. This analysis suggests that the elastic cross section plays a dominant role in the measured increase in trap loss.

5 Conclusion

In summary, we present the first measurement of cold collisions between distinct polar molecules in a variable electric field. We report absolute trap loss cross sections and electric-field enhancement of collision cross sections. Results from zero-field *ab initio* PESs are presented along with semiclassical estimates that reproduce both measured loss cross sections. A variety of OH collision partners are available from the buffer gas source, allowing for a host of future cold collision studies between chemically-interesting molecules. Furthermore, the sensitivity of this technique to elastic differential cross sections allows for direct measurement of the DCS in a trap of variable depth. Future work will include calculation of field-dependent values for $\sigma^{\rm loss}_{\rm theory}$ as well as possible detection of inelastically scattered collision products within the trap region.

Acknowledgements

The authors acknowledge DOE, AFOSR-MURI, NSF, and NIST for funding support. M. Hummon is a National Research Council postdoctoral fellow. T.V. Tscherbul was supported by NSF grants to the Harvard-MIT CUA and ITAMP at Harvard University and Smithsonian Astrophysical Observatory. We thank G. Quéméner and J. L. Bohn for stimulating discussions and J. Rasmussen for technical assistance.

References

1 *Atomic and Molecular Beam Methods*, ed. G. Scoles *et al.*, Oxford Univ. Pr., Cary, NC, USA, 1988.
2 M. C. van Beek *et al.*, *Phys. Rev. Lett.*, 2001, **86**, 4001–4004.
3 M. H. Alexander and S. Stolte, *J. Chem. Phys.*, 2000, **112**, 8017–8026.
4 M. J. L. de Lange *et al.*, *J. Chem. Phys.*, 2004, **121**, 11691–1171.
5 R. Cireasa, A. Moise and J. J. ter Meulen, *J. Chem. Phys.*, 2007, **123**, 64310.
6 C. A. Taatjes *et al.*, *J. Phys. Chem. A*, 2007, **111**, 7631–7639.
7 L. D. Carr *et al.*, *New J. Phys.*, 2009, **11**, 055049.
8 J. J. Gilijamse *et al.*, *Science*, 2006, **313**, 1617.
9 L. Scharfenberg *et al.*, *Phys. Chem. Chem. Phys.*, 2010, **12**, 10660.
10 M. Kirste *et al.*, *Phys. Rev. A*, 2010, **82**, 042717.
11 B. C. Sawyer *et al.*, *Phys. Rev. Lett.*, 2008, **101**, 203203.
12 T. V. Tscherbul *et al.*, *Phys. Rev. A*, 2010, **82**, 022704.
13 W. C. Campbell *et al.*, *Phys. Rev. Lett.*, 2007, **98**, 213001.
14 W. C. Campbell *et al.*, *Phys. Rev. Lett.*, 2009, **102**, 013003.
15 M.-J. Lu and J. D. Weinstein, *New J. Phys.*, 2009, **11**, 055015.
16 S. Willitsch *et al.*, *Phys. Rev. Lett.*, 2008, **100**, 043203.
17 K.-K. Ni *et al.*, *Science*, 2008, **322**, 231–235.
18 S. Ospelkaus *et al.*, *Science*, 2010, **327**, 853–857.
19 K. K. Ni *et al.*, *Nature*, 2010, **464**, 1324–1328.
20 A. Micheli, G. K. Brennen and P. Zoller, *Nature Physics*, 2006, **2**, 341–347.
21 K. R. Lang and R. F. Wilson, *Astrophys. J.*, 1980, **238**, 867–873.
22 J. C. McConnell, *J. Geophys. Res.*, 1973, **78**, 7812–7821.
23 T. Ridley, K. P. Lawley and R. J. Donovan, *J. Chem. Phys.*, 2009, **131**, 234302.
24 B. C. Sawyer *et al.*, *Phys. Rev. Lett.*, 2007, **98**, 253002.
25 L. D. van Buuren *et al.*, *Phys. Rev. Lett.*, 2009, **102**, 033001.
26 D. Patterson, J. Rasmussen and J. M. Doyle, *New J. Phys.*, 2009, **11**, 055018.
27 R. N. Dixon, J. M. Bayley and M. N. R. Ashfold, *Chem. Phys. Lett.*, 2000, **332**, 85–92.
28 J. R. Bochinksi *et al.*, *Phys. Rev. A*, 2004, **70**, 043410.
29 H. Cybulski *et al.*, *J. Chem. Phys.*, 2005, **122**, 094307.
30 J. Perez-Rios *et al.*, *J. Phys. Chem. A*, 2009, **113**, 14952–14960.
31 T. V. Tscherbul *et al.*, *New J. Phys.*, 2009, **11**, 055021.
32 A. R. Offer, M. C. van Hemert and E. F. van Dishoeck, *J. Chem. Phys.*, 1994, **100**, 362–378.
33 T. V. Tscherbul and J. Kłos, in preparation.
34 H. J. Werner *et al.*, MOLPRO, version 2008.1, a package of *ab initio* programs, see http://www.molpro.net.
35 P. E. S. Wormer, J. A. Kłos, G. C. Groenenboom and A. van der Avoird, *J. Chem. Phys.*, 2005, **122**, 244325.
36 T. H. Dunning, Jr., *J. Chem. Phys.*, 1989, **90**, 1007–1023.
37 K. P. Huber and G. Herzberg, *Constants of Diatomic molecules*, Van Nostrand Reinhold, New York, 1979.

38 P. S. Zuchowski and J. M. Hutson, *Phys. Rev. A*, 2009, **79**, 062708.
39 D. E. Manolopoulos, *J. Chem. Phys.*, 1986, **85**, 6425–6429.
40 V. Aquilanti *et al.*, *J. Am. Chem. Soc.*, 1999, **121**, 10794–10802.
41 D. E. Fagnan *et al.*, *Phys. Rev. A*, 2009, **80**, 022712.
42 J. J. Sakurai, *Modern Quantum Mechanics*, Addison-Wesley Publishing Co., Reading, MA, USA, 1994.
43 M. T. Bell and T. P. Softley, *Mol. Phys.*, 2009, **107**, 99–132.
44 A. Derevianko, J. F. Babb and A. Dalgarno, *Phys. Rev. A*, 2001, **63**, 052704.